Volume 17
Number 16
28 April 2025
Pages 9601-10392

Nanoscale

rsc.li/nanoscale

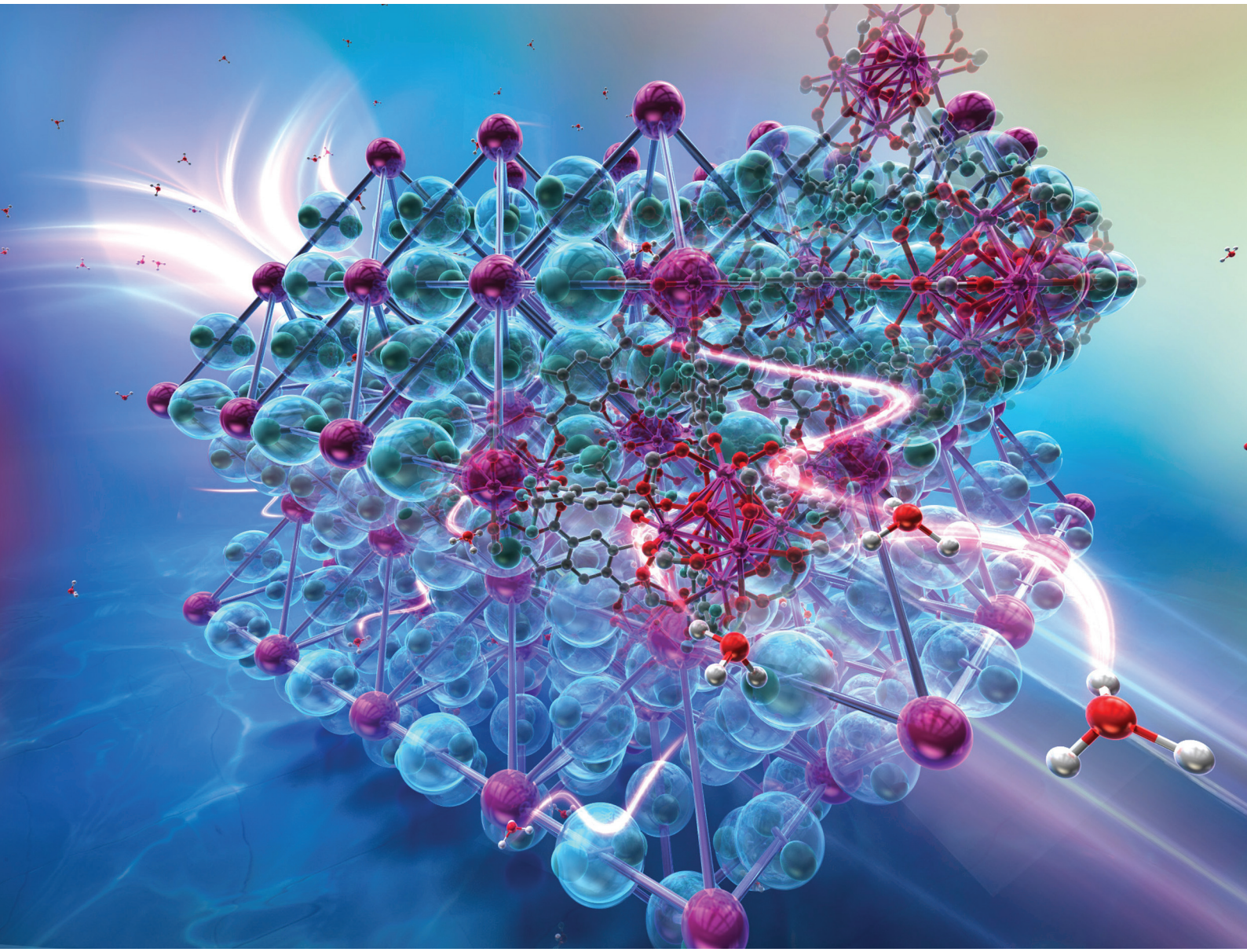

ISSN 2040-3372

ROYAL SOCIETY OF CHEMISTRY

PAPER
Ryota Akai, Kouki Oka *et al.*
Fluorinated metal–organic frameworks: hydrophobic nanospaces with high fluorine density and proton conductivity

NCNST

Nanoscale

PAPER

View Article Online
View Journal | View Issue

Cite this: *Nanoscale*, 2025, **17**, 9920

Fluorinated metal–organic frameworks: hydrophobic nanospaces with high fluorine density and proton conductivity†

Ryota Akai, [a] Hitoshi Kasai[a] and Kouki Oka *[a,b,c]

Received 23rd January 2025,
Accepted 13th March 2025

DOI: 10.1039/d5nr00342c

rsc.li/nanoscale

The current work revealed the relationship between the fluorine density of organic-based porous materials and water dynamics (proton conduction) in the hydrophobic nanospace. In detail, by focusing on UiO-66 with structural durability at high temperature/humidity based on strong Zr–O bonds, we prepared UiO-66-CF_3 and UiO-66-$(CF_3)_2$ with different fluorine densities. The activation energies for proton conduction of UiO-66-CF_3 (0.91 eV) and UiO-66-$(CF_3)_2$ (1.38 eV) were significantly larger than that in UiO-66 (0.47 eV) depending on their fluorine density. Introducing fluorine into organic-based porous materials allowed the hydrophobic nanospace to interact with protons, yielding a larger energy for proton conduction (activation energy). The fluorine density and activation energy were proportional. We clarified that the activation energy of proton conduction increased proportionally with the fluorine density in the nanospace. This indicated the possibility that the state of proton/water in the nanospace could be freely controlled by the fluorine density.

Introduction

Fluorinated organic-based materials exhibit high hydrophobicity and chemical durability owing to their specific interaction with water based on the high electronegativity of fluorine,[1,2] and are suitable for various applications, such as hydrous proton conductors,[3,4] water–oil separating materials,[5,6] and electrocatalysts.[5,7,8] Even among organic-based materials with low water resistance, those with fluorine have been extensively investigated for proton exchange membrane applications in fuel cells as hydrous proton conductors.[3,4,9] However, the relationship between fluorine density and proton conductivity within the hydrophobic nanospace constructed by fluorine introduction has not been elucidated.

Among organic-based porous materials with robust paths for proton conduction, metal–organic frameworks (MOFs) exhibit high crystallinity compared to covalent organic frameworks (COFs) and hydrogen-bonded organic frameworks (HOFs).[10–14] Moreover, MOFs maintain high crystallinity even after introducing substituents to the linkers.[10,11] Among them, UiO-66, which yields high chemical and thermal durability in water and organic solvents owing to strong Zr–O bonds,[15–18] provides a platform for elucidating structure–property relationships.[19–21] Focusing on proton conduction, Kitagawa *et al.* investigated the effect of the number of missing linkers in UiO-66 on the proton conductivity.[22] Li *et al.* investigated the effect of the acidity of the functional groups introduced into UiO-66 on the proton conductivity.[23] Li *et al.* investigated the relationship between the number of carboxy groups and proton conductivity in Ce-UiO-66 with Ce as the metal and carboxy groups as acidic functional groups.[24] We have reported that highly fluorinated HOFs exhibited high water durability and proton conductivity.[3] However, studies for improving proton conductivity by modulating the interaction with water and protons in the nanospace depending on the number of introduced fluorine substituents are limited.

In the current work, we prepared UiO-66-CF_3 and UiO-66-$(CF_3)_2$ with different numbers of fluorine atoms in the linker to change the fluorine density in the nanospaces of UiO-66. We demonstrated that introducing fluorine into organic-based porous materials allowed the hydrophobic nanospace to interact with water and protons, yielding larger energy for proton conduction (activation energy) and a predominance of the vehicle mechanism. We revealed that the fluorine density and activation energies were proportional.

[a]*Institute of Multidisciplinary Research for Advanced Materials, Tohoku University, 2-1-1 Katahira, Aoba-ku, Sendai, Miyagi 980-8577, Japan. E-mail: oka@tohoku.ac.jp*
[b]*Carbon Recycling Energy Research Center, Ibaraki University, 4-12-1 Nakanarusawa, Hitachi, Ibaraki 316-8511, Japan*
[c]*Deuterium Science Research Unit, Center for the Promotion of Interdisciplinary Education and Research, Kyoto University, Yoshida, Sakyo-ku, Kyoto 606-8501, Japan*
†Electronic supplementary information (ESI) available. See DOI: https://doi.org/10.1039/d5nr00342c

Experimental section

Preparation of UiO-66

We prepared UiO-66 with reference to a previous work.[25] $ZrCl_4$ (291 mg, 1.25 mmol) and terephthalic acid (208 mg, 1.25 mmol) were dissolved in a solution of *N*,*N*-dimethylformamide (10 mL), acetic acid (2 mL), and water (0.14 mL), and the mixture was sonicated at 20 °C for 5 min and stirred at 20 °C for 15 min. Finally, the mixture was placed in a microwave oven and irradiated at 120 °C for 15 min. The product was centrifuged, then washed with *N*,*N*-dimethylformamide and methanol, and, lastly, dried at 120 °C for 5 h, affording a white solid UiO-66 (68 mg).

Results and discussion

Preparation and characterization of UiO-66-X

As shown in Fig. 1, based on previous works,[25,26] we synthesized UiO-66-X (-X = -H, $-CF_3$, and $-(CF_3)_2$) with terephthalic acid, 2-(trifluoromethyl)terephthalic acid, and 2,5-bis(trifluoromethyl)terephthalic acid as linker molecules, respectively, by a microwave method (the details are described in the Experimental section). Fig. S1† supports the introduction of trifluoromethyl groups in UiO-66-CF_3 and UiO-66-$(CF_3)_2$. UiO-66-X were activated under vacuum at 120 °C for 5 h. As shown in Fig. S2,† all solvents used in the preparation of UiO-66-X were completely removed. As shown in the scanning electron microscopy (SEM) images in Fig. 1, the particle sizes of UiO-66, UiO-66-CF_3, and UiO-66-$(CF_3)_2$ were about 200 nm, 200 nm, and 50–200 nm, respectively.

In this section, we have characterized UiO-66-X. As shown in Fig. 2a and Table S1,† the Brunauer–Emmett–Teller (BET) specific surface area and pore volume of UiO-66-X were evaluated based on the adsorption/desorption isotherms of N_2 at 77 K. As shown in Table S1,† the BET specific surface areas of UiO-66-X (-X = -H, $-CF_3$, and $-(CF_3)_2$) were 2143 ($\times 10^3$ m^2 mol^{-1}), 1825 ($\times 10^3$ m^2 mol^{-1}), and 970 ($\times 10^3$ m^2 mol^{-1}), respectively. As shown in Fig. S3 and Table S1,† the pore volumes were 2220 (cm^3 mol^{-1}), 1836 (cm^3 mol^{-1}), and 395 (cm^3 mol^{-1}), respectively. As shown in the powder X-ray diffraction (PXRD) analysis in Fig. 2b, UiO-66-X (-X = -H, $-CF_3$, and $-(CF_3)_2$) were isostructural, and therefore, as shown in Table S1,† their BET specific surface area and pore volume decreased according to the number of introduced trifluoromethyl groups. Fig. 2c and Table S2† depict Fourier transform infrared (FT-IR) spectra, in which four peaks at 1610 cm^{-1}, 1410 cm^{-1}, 1363 cm^{-1}, and 1067 cm^{-1} were observed for UiO-66-X (-X = -H, $-CF_3$, and $-(CF_3)_2$). These originate from COO^- units.[24] The peak at 1520 cm^{-1} was attributed to C=C bonds of benzene rings.[27] Three peaks at 1300 cm^{-1}, 1273 cm^{-1}, and 1140 cm^{-1}, which were observed only for UiO-66-CF_3 and UiO-66-$(CF_3)_2$, were ascribed to the C–F bond.[28,29] Two peaks at 909 cm^{-1} and 744 cm^{-1} were due to C–H bonds.[30] Two peaks at 661 cm^{-1} and 604 cm^{-1} were attributed to Zr–$O_{\mu 3\text{-}O}$ and Zr–(OC) bonds.[27] The broad peak between 3000 cm^{-1} and 3500 cm^{-1} originated from absorbed water.[27] Since UiO-66-X usually has missing linkers,[20] as shown in Fig. S4,† the percentages of missing linkers were evaluated based on thermogravimetric analysis (TGA) (the details are described in section 2.3 of the ESI).† Defect-free UiO-66-X had six linkers per Zr cluster. UiO-66-X (X = -H, $-CF_3$, and $-(CF_3)_2$) had 3.26 (-H), 4.58 ($-CF_3$), and 4.21 ($-(CF_3)_2$) linkers, respectively. Introducing electron-withdrawing substituents into terephthalic acid enabled a smaller pK_a of the carboxy group[31] and easier coordination to Zr, yielding fewer structural defects in UiO-66-CF_3 than in UiO-66 despite the similar synthesis conditions. Two isostructural UiO-66-X materials with different fluorine densities were successfully prepared.

Water vapor adsorption properties of UiO-66-X

To confirm whether water molecules can penetrate the hydrophobic nanospaces created by trifluoromethyl groups introduced into UiO-66, as shown in Fig. 3 and S6,† water vapor adsorption/desorption measurements were performed at 298 K. At high relative pressure ($P_e/P_0 > 0.80$), UiO-66-X (-X = -H, $-CF_3$, and $-(CF_3)_2$) readily adsorbed water vapor. The significant increases in the adsorption in the first step where $0.30 < P_e/P_0 < 0.40$ were attributable to water vapor clusters formed on the nanospace surfaces.[32] The significant increases in adsorption in the second step where $P_e/P_0 > 0.97$ were attributable to the liquefaction of the adsorbed water vapor.[33]

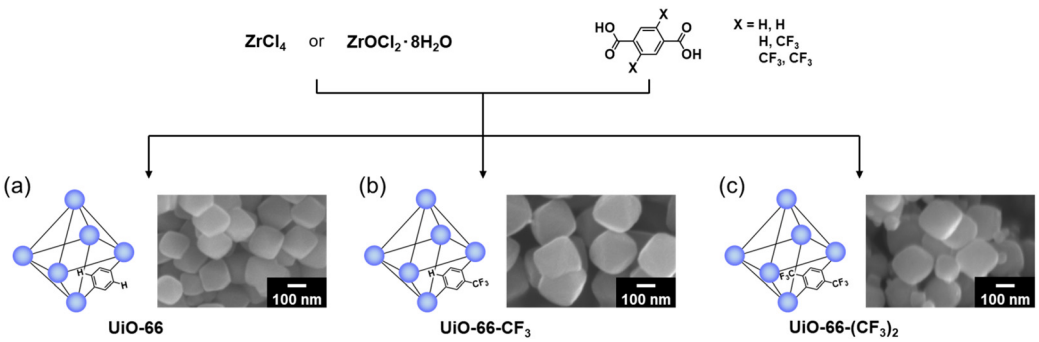

Fig. 1 Preparation and scanning electron microscopy (SEM) images (scale bar: 100 nm) of (a) UiO-66, (b) UiO-66-CF_3, and (c) UiO-66-$(CF_3)_2$.

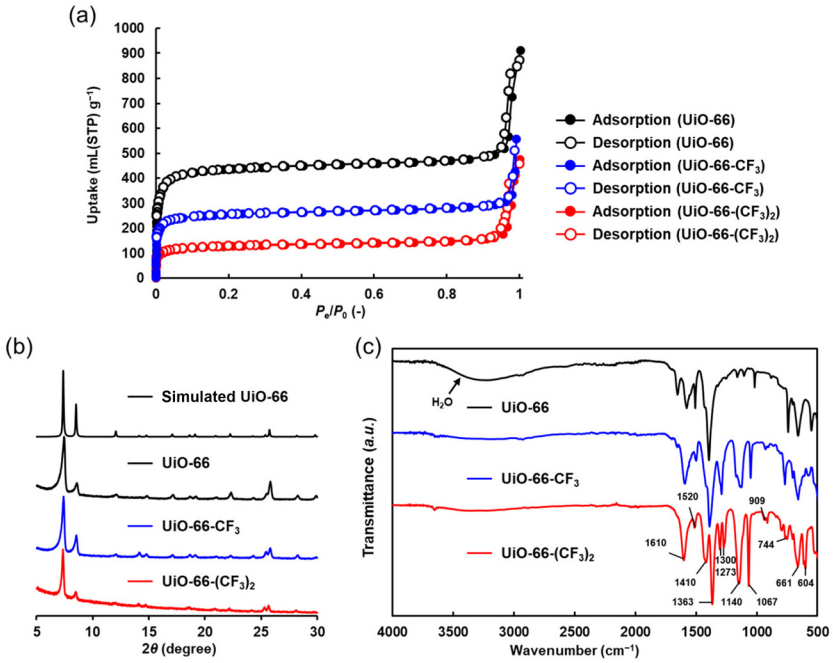

Fig. 2 (a) N_2 adsorption/desorption isotherms of UiO-66 (black), UiO-66-CF_3 (blue), and UiO-66-$(CF_3)_2$ (red) at 77 K. Their crystallinity was maintained after N_2 adsorption (Fig. S5†). (b) PXRD patterns of simulated UiO-66 (upper black), UiO-66 (lower black), UiO-66-CF_3 (blue), and UiO-66-$(CF_3)_2$ (red). (c) FT-IR spectra of UiO-66 (black), UiO-66-CF_3 (blue), and UiO-66-$(CF_3)_2$ (red).

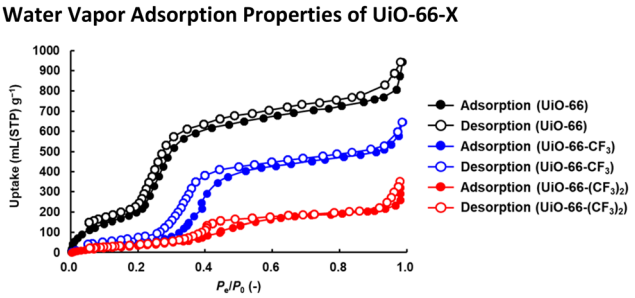

Fig. 3 Water vapor adsorption/desorption isotherms of UiO-66 (black), UiO-66-CF_3 (blue), and UiO-66-$(CF_3)_2$ (red) at 298 K. Their crystallinity was maintained after water vapor adsorption (Fig. S5†).

It should be noted, as shown in Fig. S6,† that the adsorption in the first step by UiO-66-CF_3 and UiO-66-$(CF_3)_2$ occured at higher relative pressure ($P_e/P_0 > 0.30$) compared to UiO-66, while first-step adsorption for UiO-66-$(CF_3)_2$ with the highest fluorine density occured at $P_e/P_0 \approx 0.40$. Since the pore surface adsorbed water molecules sequentially from the more hydrophilic areas, the higher the hydrophobicity (fluorine density) of the pore surface, the higher the pressure required for water vapor adsorption.[34] In other words, the larger the hydrophobic portion of the total pore surface, the less water vapor was adsorbed at low pressure, and the higher the pressure threshold for the first step of water vapor adsorption depending on the hydrophobicity of the pore surface. Since the trifluoromethyl groups introduced into UiO-66 were exposed on the pore surface based on the crystal structure of UiO-66,[35] the hydrophobic portion of the total pore surface increased proportionally with fluorine density. Therefore, as shown in Fig. S7,† the pressure threshold for the first step of water vapor adsorption increased proportionally with fluorine density of UiO-66-X, indicating that the nanospaces have become more hydrophobic.[32,36]

Proton conductivity of UiO-66-X

As shown in Fig. 4a–c, the proton conductivities (σ_X) of pelletized UiO-66-X were measured by electrochemical impedance spectroscopy (EIS). The proton conductivities were calculated by fitting analysis assuming the equivalent circuit shown in Fig. S8.† As shown in Fig. 4a–c, dielectric relaxation in the high-frequency region indicated that the proton conductivities of UiO-66-X (-X = -H, -CF_3, and -$(CF_3)_2$) under 95% relative humidity (RH) at 30 °C were $\sigma_H = 3.34 \times 10^{-4}$ S cm^{-1}, $\sigma_{CF_3} = 5.67 \times 10^{-7}$ S cm^{-1}, and $\sigma_{(CF_3)_2} = 3.34 \times 10^{-6}$ S cm^{-1}, respectively. As shown in Fig. S9,† the direct current (DC) electrical conductivity values calculated from DC resistance of UiO-66-X (-X = -H, -CF_3, and -$(CF_3)_2$) were 4.59×10^{-9} S cm^{-1}, 2.14×10^{-9} S cm^{-1}, and 1.44×10^{-9} S cm^{-1} under 95% RH at 30 °C, respectively. These values were much lower than those of σ_X, supporting σ_X as the proton conductivities of UiO-66-X. The coordinated water in the metal cluster site could be a proton source for proton conduction owing to partial dissociation caused by the Lewis acidity of the metal ions, yielding a lower pK_a than that of pure water.[24,37,38]

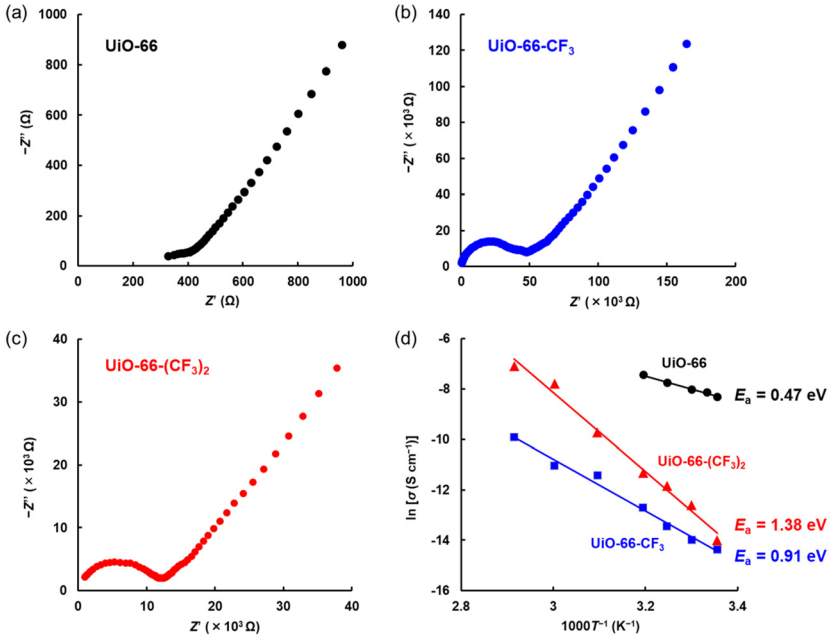

Fig. 4 Cole–Cole plots of (a) UiO-66, (b) UiO-66-CF_3, and (c) UiO-66-$(CF_3)_2$. Impedance spectrum of the disk-shaped pellet under 95% RH at 30 °C. (d) Arrhenius plots of proton conductivity under 95% RH. R^2 values of UiO-66, UiO-66-CF_3, and UiO-66-$(CF_3)_2$ were 0.994, 0.987, and 0.989, respectively. As shown in Fig. 1, small particles of UiO-66-$(CF_3)_2$ less than 200 nm were also produced, suggesting a slight decrease in proton conductivity.[39]

In UiO-66, a smaller σ value was reported for hydrophobic nanospaces where halogen substituents without proton-donating ability were introduced into the linker.[23] A larger σ value was reported for a larger number of missing linkers in UiO-66.[22] Therefore, σ_{CF_3} and $\sigma_{(CF_3)_2}$ would have been smaller than σ_H. Introducing trifluoromethyl groups into the linker caused the pK_a of the C–H of the benzene ring to follow the order p$K_a((CF_3)_2)$ < p$K_a(CF_3)$.[40] Thus, smaller pK_a values yield larger σ values;[41] therefore, the proton conductivity was $\sigma_{(CF_3)_2} > \sigma_{CF_3}$.

As shown in the Arrhenius plots in Fig. 4d, the activation energies (E_a) of UiO-66, UiO-66-CF_3, and UiO-66-$(CF_3)_2$ were $E_a(H)$ = 0.47 eV, $E_a(CF_3)$ = 0.91 eV, and $E_a((CF_3)_2)$ = 1.38 eV, respectively. The proton conduction mechanisms differed depending on E_a and were classified as being either Grotthuss (E_a < 0.4 eV) or vehicle mechanisms (E_a > 0.5 eV).[41,42] The Arrhenius plots shown in Fig. 4d indicated that UiO-66 followed the intermediate process between the Grotthuss and vehicle mechanisms (mainly vehicle mechanism),[42] while UiO-66-CF_3 and UiO-66-$(CF_3)_2$ followed the vehicle mechanism. UiO-66-CF_3 and UiO-66-$(CF_3)_2$ could not form strong hydrogen bonding networks, like sulfo and carboxy groups,[23] and the vehicle mechanism was predominant. Since the percentage of missing linkers in UiO-66 has been reported to have little effect on E_a,[22] the fluorine density was considered to be mainly affected by E_a. The number of hydrogen bonds formed/broken when a proton moved a certain distance was proportional to the fluorine density. Therefore, as shown in Fig. S10,† the fluorine density and E_a exhibited a proportional relationship.

Conclusions

In the current work, we revealed the relationship between the fluorine density of organic-based porous materials and water dynamics (proton conduction) in the hydrophobic nanospace. In detail, focusing on UiO-66 with structural durability at high temperature/humidity based on strong Zr–O bonds, we prepared UiO-66-CF_3 and UiO-66-$(CF_3)_2$ with different numbers of trifluoromethyl groups in the linker to change the fluorine density per unit volume, respectively. Compared to UiO-66, the hydrophobicity in nanospaces of UiO-66-CF_3 and UiO-66-$(CF_3)_2$ were increased depending on their fluorine density owing to the higher relative pressure where steep adsorption in the first step occurred. The activation energies for proton conduction of UiO-66-CF_3 (0.91 eV) and UiO-66-$(CF_3)_2$ (1.38 eV) were significantly larger than that in UiO-66 (0.47 eV) depending on their fluorine densities rather than the percentage of missing linkers. We demonstrated for the first time that introducing fluorine into organic-based porous materials allowed the hydrophobic nanospace to interact with water and protons, yielding a larger energy for proton conduction (E_a) and a predominance of the vehicle mechanism. The results revealed that, despite the small number of samples and the initial results, fluorine density and activation energy were proportional. We clarified that the activation energy of proton conduction increased proportionally with the fluorine density in the nanospace. This indicated the possibility that the state of proton/water in the nanospace could be freely controlled by the fluorine density. In our continuous work, we elucidated the detailed mechanism of proton conduction (*e.g.* vehicle or

Grotthuss mechanism) by quasi-elastic neutron scattering and molecular dynamics simulation based on the crystal structures. The more detailed relationship between fluorine density and activation energy of proton conduction can be corroborated by using other UiO-66 derivatives such as UiO-66-F, UiO-66-F_2 and UiO-66-F_4.

Author contributions

Ryota Akai: conceptualization, methodology, formal analysis, data curation, investigation, writing – original draft, funding acquisition, and resources. Hitoshi Kasai: writing – review & editing. Kouki Oka: conceptualization, methodology, formal analysis, data curation, project administration, validation, supervision, writing – original draft, writing – review & editing, funding acquisition, resources, and software.

Data availability

The data supporting this article have been included as part of the ESI.†

Conflicts of interest

There are no conflicts to declare.

Acknowledgements

This work was partially supported by Grants-in-Aid for Scientific Research (no. JP23K17945, JP23H03827, JP24K01552, and JP24KJ1576) from MEXT, Japan. This work was supported by JSPS Bilateral Program Number JPJSBP120258801. This work was partially supported by the Environment Research and Technology Development Fund (JPMEERF20241RA4) of the Environmental Restoration and Conservation Agency provided by the Ministry of the Environment of Japan. K. O. also acknowledges the support from the Shorai Foundation for Science and Technology, TEPCO Memorial Foundation, Amano Industry Technology Laboratory, Sugiyama Houkoukai, the Yamada Science Foundation, Kenjiro Takayanagi Foundation, the Kansai Research Foundation for Technology Promotion, the Yashima Environment Technology Foundation, JACI Prize for Encouraging Young Researcher, Iketani Science and Technology Foundation, Foundation for Interaction in Science & Technology, and Ozawa and Yoshikawa Memorial Electronics Research Foundation. R. A. also acknowledges the support from the Hosokawa Powder Technology Foundation and the Mishima Kaiun Memorial Foundation.

References

1 R. Berger, G. Resnati, P. Metrangolo, E. Weber and J. Hulliger, *Chem. Soc. Rev.*, 2011, **40**, 3496–3508.
2 S. Kumar, B. Mohan, C. Fu, V. Gupta and P. Ren, *Coord. Chem. Rev.*, 2023, **476**, 214876.
3 T. Ami, K. Oka, S. Kitajima and N. Tohnai, *Angew. Chem., Int. Ed.*, 2024, **63**, e202407484.
4 P. G. M. Mileo, K. Adil, L. Davis, A. Cadiau, Y. Belmabkhout, H. Aggarwal, G. Maurin, M. Eddaoudi and S. Devautour-Vinot, *J. Am. Chem. Soc.*, 2018, **140**, 13156–13160.
5 W.-B. Li, Y.-Z. Cheng, D.-H. Yang, Y.-W. Liu and B.-H. Han, *Macromol. Rapid Commun.*, 2023, **44**, 2200778.
6 Y. Liu, Z. Lin, Y. Luo, R. Wu, R. Fang, A. Umar, Z. Zhang, Z. Zhao, J. Yao and S. Zhao, *J. Cleaner Prod.*, 2023, **420**, 138347.
7 M. Chatenet, S. Berthon-Fabry, Y. Ahmad, K. Guérin, M. Colin, H. Farhat, L. Frezet, G. Zhang and M. Dubois, *Adv. Energy Mater.*, 2023, **13**, 2204304.
8 J. Wang, R. Abazari, S. Sanati, A. Ejsmont, J. Goscianska, Y. Zhou and D. P. Dubal, *Small*, 2023, **19**, 2300673.
9 S. Siracusano, C. Oldani, M. A. Navarra, S. Tonella, L. Mazzapioda, N. Briguglio and A. S. Aricò, *J. Membr. Sci.*, 2019, **578**, 136–148.
10 S. K. Bhardwaj, N. Bhardwaj, R. Kaur, J. Mehta, A. L. Sharma, K.-H. Kim and A. Deep, *J. Mater. Chem. A*, 2018, **6**, 14992–15009.
11 Z. Chen, X. Li, C. Yang, K. Cheng, T. Tan, Y. Lv and Y. Liu, *Adv. Sci.*, 2021, **8**, 2101883.
12 M. Åhlén, O. Cheung and C. Xu, *Dalton Trans.*, 2023, **52**, 1841–1856.
13 C.-Y. Xiao, T.-Y. Chen, R.-J. Chung, S. Yougbaré, L.-Y. Lin and Y.-F. Wu, *J. Energy Storage*, 2022, **55**, 105622.
14 R. Medishetty, J. K. Zaręba, D. Mayer, M. Samoć and R. A. Fischer, *Chem. Soc. Rev.*, 2017, **46**, 4976–5004.
15 E.-S. M. El-Sayed, Y. D. Yuan, D. Zhao and D. Yuan, *Acc. Chem. Res.*, 2022, **55**, 1546–1560.
16 C. Xiao, J. Tian, Q. Chen and M. Hong, *Chem. Sci.*, 2024, **15**, 1570–1610.
17 X. Zhang, B. Wang, A. Alsalme, S. Xiang, Z. Zhang and B. Chen, *Coord. Chem. Rev.*, 2020, **423**, 213507.
18 Y. J. Kim, S. Y. Ko, S. Kim, K. M. Choi and W.-H. Ryu, *Small*, 2023, **19**, 2206561.
19 F. Ahmadijokani, H. Molavi, M. Rezakazemi, S. Tajahmadi, A. Bahi, F. Ko, T. M. Aminabhavi, J.-R. Li and M. Arjmand, *Prog. Mater. Sci.*, 2022, **125**, 100904.
20 J. Winarta, B. Shan, S. M. McIntyre, L. Ye, C. Wang, J. Liu and B. Mu, *Cryst. Growth Des.*, 2020, **20**, 1347–1362.
21 D. Zou and D. Liu, *Mater. Today Chem.*, 2019, **12**, 139–165.
22 J. M. Taylor, S. Dekura, R. Ikeda and H. Kitagawa, *Chem. Mater.*, 2015, **27**, 2286–2289.
23 F. Yang, H. Huang, X. Wang, F. Li, Y. Gong, C. Zhong and J.-R. Li, *Cryst. Growth Des.*, 2015, **15**, 5827–5833.
24 H.-M. Ren, B.-Y. Liu, B.-T. Zuo, Z.-F. Li and G. Li, *Microporous Mesoporous Mater.*, 2023, **351**, 112481.
25 M. Taddei, P. V. Dau, S. M. Cohen, M. Ranocchiari, J. A. van Bokhoven, F. Costantino, S. Sabatini and R. Vivani, *Dalton Trans.*, 2015, **44**, 14019–14026.

26 H. Reinsch, S. Waitschat, S. M. Chavan, K. P. Lillerud and N. Stock, *Eur. J. Inorg. Chem.*, 2016, **2016**, 4490–4498.
27 Y. L. Wang, S. Zhang, Y. F. Zhao, J. Bedia, J. J. Rodriguez and C. Belver, *J. Environ. Chem. Eng.*, 2021, **9**, 106087.
28 Z. Zhou, X. Cao, D. Lv and F. Cheng, *Sep. Purif. Technol.*, 2024, **339**, 126666.
29 I. Das and G. De, *Sci. Rep.*, 2015, **5**, 18503.
30 R. A. Espinosa-Flores, M. D. Trejo-Valdez, M. E. Manríquez-Ramírez and F. J. Tzompantzi-Morales, *Heliyon*, 2023, **9**, e17138.
31 C. A. Hollingsworth, P. G. Seybold and C. M. Hadad, *Int. J. Quantum Chem.*, 2002, **90**, 1396–1403.
32 B. Zhang, Z. Zhu, X. Wang, X. Liu and F. Kapteijn, *Adv. Funct. Mater.*, 2024, **34**, 2304788.
33 Y. Byun, S. H. Je, S. N. Talapaneni and A. Coskun, *Chem. – Eur. J.*, 2019, **25**, 10262–10283.
34 A. Metrane, A. Delhali, M. Ouikhalfan, A. H. Assen and Y. Belmabkhout, *J. Chem. Eng. Data*, 2022, **67**, 1617–1653.
35 C. A. Trickett, K. J. Gagnon, S. Lee, F. Gándara, H.-B. Bürgi and O. M. Yaghi, *Angew. Chem., Int. Ed.*, 2015, **54**, 11162–11167.
36 E.-P. Ng and S. Mintova, *Microporous Mesoporous Mater.*, 2008, **114**, 1–26.
37 N. C. Jeong, B. Samanta, C. Y. Lee, O. K. Farha and J. T. Hupp, *J. Am. Chem. Soc.*, 2012, **134**, 51–54.
38 H. Ōkawa, A. Shigematsu, M. Sadakiyo, T. Miyagawa, K. Yoneda, M. Ohba and H. Kitagawa, *J. Am. Chem. Soc.*, 2009, **131**, 13516–13522.
39 D. A. Levenson, J. Zhang, B. S. Gelfand, S. P. Kammampata, V. Thangadurai and G. K. H. Shimizu, *Dalton Trans.*, 2020, **49**, 4022–4029.
40 K. Shen, Y. Fu, J.-N. Li, L. Liu and Q.-X. Guo, *Tetrahedron*, 2007, **63**, 1568–1576.
41 A. Shigematsu, T. Yamada and H. Kitagawa, *J. Am. Chem. Soc.*, 2011, **133**, 2034–2036.
42 X. Meng, H.-N. Wang, S.-Y. Song and H.-J. Zhang, *Chem. Soc. Rev.*, 2017, **46**, 464–480.